Structure of a Transition Metal-Containing Polyyne

A. E. Dray,*,† R. Rachel,‡ W. O. Saxton,§ J. Lewis,⊥ M. S. Khan,⊥ A. M. Donald,† and R. H. Friend†

Cavendish Laboratory, University of Cambridge, Madingley Road, Cambridge, CB3 0HE, U.K., Lehrstuhl für Mikrobiologie, Universität Regensburg, D-8400 Regensburg, Germany, Department of Materials Science and Metallurgy, University of Cambridge, Pembroke Street, Cambridge, CB2 3QZ, U.K., and University Chemical Laboratory, University of Cambridge, Lensfield Road, Cambridge, CB2 1EW, U.K.

Received September 11, 1991; Revised Manuscript Received February 18, 1992

ABSTRACT: Electron diffraction and low-dose, high-resolution imaging techniques have been used to obtain structural information for a rigid-rod polyyne containing platinum atoms directly bonded into the main chain. The high-resolution images show details of the arrangement of the molecular chains into crystallites ~50 nm in diameter; dislocations and grain boundaries have also been imaged. A combination of electron diffraction and information derived from image processing of the high-resolution images indicates a unit cell in which parameters of a = 2.08 nm, c = 1.20 nm, and $90° \leq \beta \leq 93°$ have been measured and where b has tentatively been assigned as ~1.9 nm. The variations in β relate to improvements in the degree of orientation of the polymer chains that arise from slight stretching of the thin films.

Introduction

Organometallic materials have attracted much interest in recent years due to their potential applications in molecular electronics, catalysis, and nonlinear optics. The material studied in the present work is one of a class of rigid-rod polymers in which the transition metal moieties are directly bonded to the conjugated organic sections of the main chain; this type of polyyne was first synthesized by Takahashi et al.,[1] and preliminary data on the polymer structures were given by Hagihara et al.[2] Initial results from our studies of these materials have been reported elsewhere;[3] details are given here of further work on the structure of these polymers.

The technique of high-resolution electron microscopy (HREM) has been applied to numerous materials science problems requiring the understanding of structure and structural defects at the atomic or molecular level and has also found use in studies of biological materials[4,5] and organic crystals.[6-10] High-resolution studies of polymeric materials have been reported by various workers.[11-17] HREM has the potential to elucidate the details of local structure, defects, and chain conformations in those crystalline polymers which will withstand the electron doses required for high-resolution imaging and which can be produced as thin films suitable for electron microscopy. We report here the preliminary results from a high-resolution study of a transition metal-containing polyyne using low-dose techniques based on those developed by Unwin and Henderson.[4]

The type of polymer used in this study was first synthesized by Takahashi et al.[1] to give a rigid-rod molecule with a weight-average molecular weight of around 30 000. Using a new, Sn-based synthesis route,[18,19] the efficiency of the reaction has been improved and polymer with a weight-average molecular weight of around 70 000 has been produced. The results presented here are for a platinum–arsenic version of the polyyne. The molecular weight was calculated from light scattering and viscosity measurements;[20] polydispersity is known to be low as fractional precipitation was used during the synthesis, and this was confirmed by ultracentrifuge sedimentation.[21] The structure of the repeat unit is

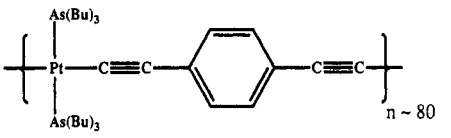

where $n \sim 80$ and the main-chain repeating length is ~1.2 nm. Alternative polymers with the Pt replaced by Pd or Ni and the As by P have also been synthesized.[19]

The main chain incorporates Pt atoms in square-planar coordination directly bonded to carbon via σ-bonds every 1.2 nm;[2] it was anticipated that the inclusion of heavy metal atoms would greatly increase the scattering of electrons in comparison to that from other organic materials. The conjugated nature of the chain would be expected to improve the stability of the polymer in the electron microscope as energy can be dissipated along the extended electron system; this polymer would thus appear to be an ideal candidate for electron microscopy although in practice there were significant beam damage problems as will be described later.

The molecules are expected to be rigid rods as a result of the nature of the bonding within the chain but flexible butyl groups bonded to the As atoms confer solubility in common organic solvents such as toluene and dichloromethane, thus permitting characterization and processing of the polymer. Attempts to grow single crystals of the polymers and oligomers suitable for X-ray diffractometry were not successful, and so all the structural information has been gleaned from electron microscopy studies.

Experimental Section

Thin films suitable for electron microscopy were cast directly onto water from 1% dichloromethane solutions and picked up on copper grids covered with a carbon support film. Film thicknesses were generally around 20 nm (measured via ellipsometry and electron energy loss spectroscopy), and selected-area diffraction patterns (SADP's) from areas of approximately 5 μm in diameter showed good overall orientation and crystallinity, as shown in Figure 1. Smaller areas showed fewer but somewhat sharper reflections as shown in Figure 2.

† Cavendish Laboratory, University of Cambridge.
‡ Lehrstuhl für Mikrobiologie, Universität Regensburg.
§ Department of Materials Science and Metallurgy, University of Cambridge.
⊥ University Chemical Laboratory, University of Cambridge.

0024-9297/92/2225-3473$03.00/0

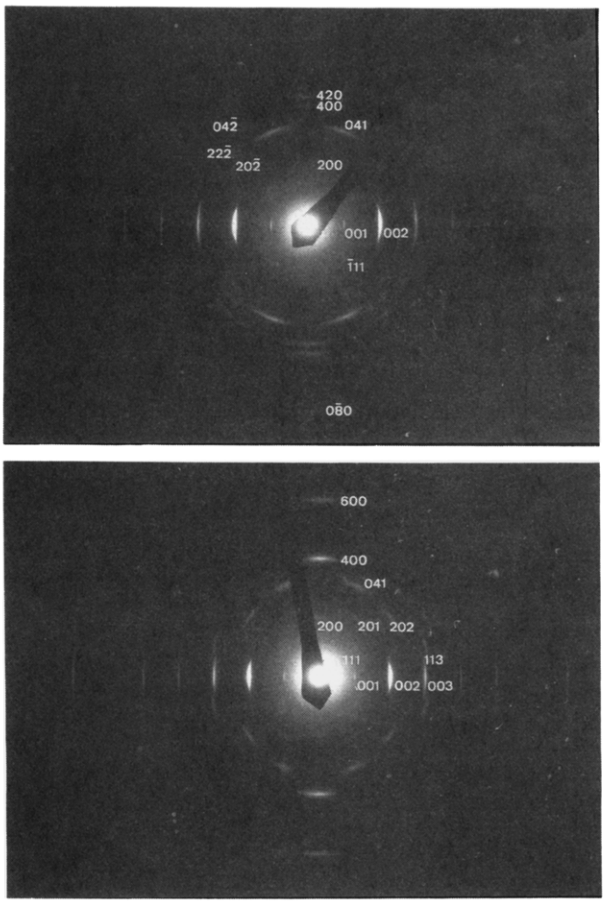

Figure 1. Selected-area diffraction patterns from large (~5-μm diameter) areas of specimen showing good orientation. The two strongest reflections (along the z^* axis, shown horizontally) are from {002}. Note the the presence of weak {001} reflections. The x^* axis is roughly perpendicular to the z^* axis. (a) Very lightly stretched region in which some crystallites were rotated about the z axis, giving rise to some hkl reflections in the $h0l$ plane. (b) More strongly stretched region showing better orientation as indicated by smaller arcs and fewer, weaker hkl reflections.

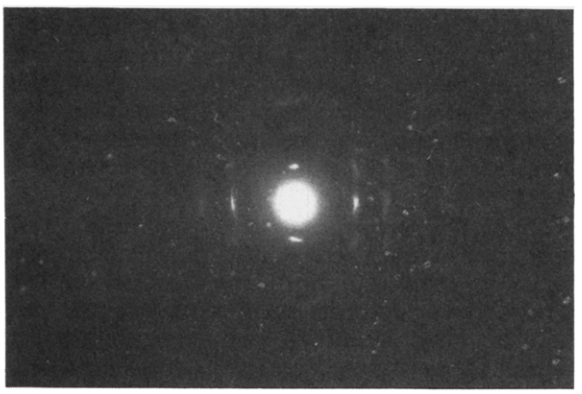

Figure 2. Selected-area diffraction pattern from a 0.5-μm-diameter area of specimen (i.e., still including several microcrystallites) showing somewhat sharper spots and fewer reflections. Same orientation as Figure 1.

All the films gave bright, crisp diffraction patterns in the electron microscope but these were found to fade rapidly with time, thus indicating that the polymer was extremely beam sensitive despite the hoped for stability deriving from the conjugated nature of the chains. Three approaches were taken to minimize beam damage, as described below.

Measurement and Minimization of the Specimen Dose and Dose Rate. Throughout this work the dose rate at the specimen has been estimated from the current falling on the fluorescent screen of the electron microscope with the beam passing through a hole in the sample. These figures will not be absolutely accurate as they do not include a factor to account for backscattering from the fluorescent screen but they do allow for the reproduction of conditions and provide a reasonable order of magnitude figure for comparison with other work.

For general survey work at room temperature the electron dose was reduced to around 10 e nm^{-2} s^{-1}. This figure was insufficient for recording images, even at low magnifications, but gave observable and recordable selected-area diffraction patterns. A critical dose for total fading of the diffraction pattern of around 200 e nm^{-2} was found at room temperature for an accelerating voltage of 200 kV on a Jeol 2000 EX transmission electron microscope.

Use of a Liquid Nitrogen Cooled Specimen Holder. All the high-resolution work described here was carried out on a Philips CM12ST transmission electron microscope using a Gatan liquid nitrogen cooled specimen holder. At room temperature on this microscope at 120 kV a critical dose for total loss of the sharp diffraction spots was ~300 e nm^{-2}, i.e., considerably higher than at 200 kV on the Jeol 2000 EX and reversing the normal trend of damage increasing at lower voltages. The CM12ST had been modified to include an additional cold trap, thus minimizing the water vapor concentration around the specimen. It is believed that the clean vacuum was responsible for the apparent increase in stability at 120 kV as compared to 200 kV on a different microscope; i.e., beam damage in this material is enhanced by chemical interactions with water and/or other contaminants.

At liquid nitrogen temperatures the critical dose increased to >3000 e nm^{-2}. This dramatic improvement in stability was unexpected as typical improvements for biological materials are generally in the range of a factor of 2–5.[22] This implies that most of the loss of crystallinity in this material resulted from secondary processes (thermal diffusion, cross-linking, reactions with radicals, etc.), as these may be minimized by cooling, whereas the extent of primary damage processes (molecular excitations and ionizations) is not a function of temperature.[23] It is likely that the observed beam damage resulted from the diffusion of and reactions with fragments of the unconjugated butyl chains which would be expected to damage readily. Beam damage in this material is considered in more detail elsewhere.[24]

Use of a Low-Dose Beam Deflection System. The critical dose for the specimens at liquid nitrogen temperatures was found to be just sufficient to expose a negative at magnifications between 50 000× and 75 000× for 1 s. Longer exposure times at lower electron doses are not desirable in cryomicroscopy as problems with specimen drift and vibration are likely to degrade the image resolution.

Focusing and astigmatism corrections were carried out on areas adjacent to those to be recorded by first deflecting the beam to one side using the low-dose imaging system on the CM12ST transmission electron microscope. Areas of interest were located by searching in the selected-area diffraction mode with a very low dose rate at the sample (≤20 e nm^{-2} compared to ~3000 e nm^{-2} during the exposure). Excluding the search dose, the high-resolution areas were only exposed for the duration of the exposure itself plus a 0.1-s stabilization time before the photographic shutter was opened.

Micrographs were recorded on Agfa Scientia film (23D56) and developed in Ilford PQ Universal (1+9) for 5 min. A 1-s high-resolution exposure corresponded to just over half of the exposure level that would normally be used for bright-field imaging and thus the contrast on the film was low but still quite adequate for viewing, enlarging, or digitizing the images. Some images were recorded on Kodak TMAX 400 film. This was found to require ε 1 exposure time of between one-fifth and one-quarter of that for the 23D56 but is more difficult to work with as it is not supplied in the correct format for TEM and must be processed in complete darkness.

High-Resolution Imaging and Image Processing. The approach taken to HREM and image interpretation in this work was based on that by Unwin and Henderson[4] in which the image is treated as a simple function of the two-dimensional projection of the original structure but where the phases and amplitudes of the diffracted beams carrying the structural information have been modified by a function which describes the distorting effects of the objective lens of the microscope. This function, the contrast

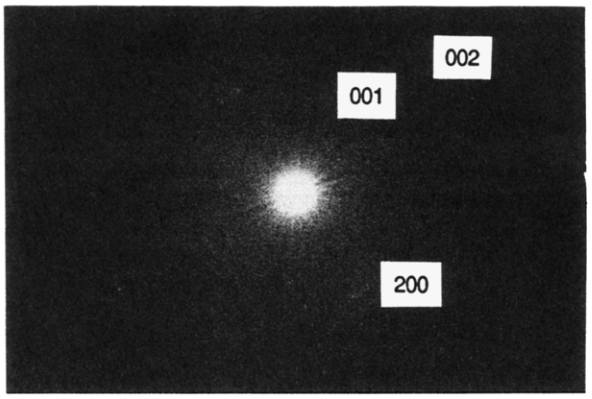

Figure 3. Optical diffractogram from a ~100-nm-diameter area of specimen. The pattern was recorded from an area of the micrograph showing good high-resolution information.

transfer function (CTF), may be written as $-2 \sin \chi$, where

$$\chi = \frac{2\pi}{\lambda}(\Delta f \theta^2/2 - C_s\theta^4/4)$$

Δf is the amount of underfocus, λ is the electron wavelength, θ is the scattering angle, and C_s is the spherical aberration coefficient of the objective lens. In practice, averaging over a range of focus levels and incident beam directions leads to additional attenuation, especially for high-order beams, but this treatment is acceptable to a first approximation.

The value of the CTF varies across the diffraction pattern, and thus the phases and amplitude of each diffracted beam must be determined individually. The value of the CTF for each beam can be deduced from optical diffractograms of the image or from the computed Fourier power spectrum of a digitized image, which shows the *square* of the CTF. Phases may be assigned easily using this approach. Diffracted amplitudes should be measured from electron diffraction patterns; in this work we have checked the phase assignment but not corrected the amplitudes as the relative intensities of the diffracted and unscattered beams are difficult to measure with certainty from the diffraction patterns obtained from these specimens. Correct phase assignment is required to ascertain the true relative positions of electron-dense areas in the image and thus in the original structure. However, in a case such as this, where information can only be recorded to very poor resolution and where accurate amplitudes cannot be measured, use of the reconstructions to generate structural models must be approached with caution.

The treatment given here assumes that multiple electron scattering can be neglected, i.e., that the specimen is a weak phase object. This assumption is valid if the extinction distances, ξ_g, for the diffracted beams contributing to the final image are significantly less than the thickness of the specimen. Calculations of ξ_g for the unit cell derived from this work based on the positions of the Pt and As atoms indicate values in excess of 400 nm. Thus, for the ≤20-nm-thick samples used, the approach appears to be valid. The details of the weak phase object approximation are covered in more depth by Unwin and Henderson and also by standard texts on high-resolution transmission electron microscopy.[23,25]

Images were first screened using an optical diffractometer to select areas with strong high-resolution information; a typical optical diffractogram is shown in Figure 3. These areas were then digitized on an Eikonix 1412 automatic densitometer using a probe diameter of 7.5 μm, which corresponded to an interval of about 0.1 nm on the micrographs recorded at 73 000×. Further selection of microcrystalline areas with strong structural information for processing was made in the Semper image processing system[26] followed by Fourier filtering and Fourier synthesis of the images.

Prior to Fourier filtration or synthesis the power spectrum of a large area of the image was calculated with Semper and the positions of the reflections were noted with respect to the peaks in the CTF; values of focus of 530 ± 7 nm underfocus and astigmatism 150 ± 7 nm were obtained for the CTF. This large degree of defocus arose from changes in the lens currents between the focus (180 000×) and exposure (73 000×) settings in the low-dose system on the CM12ST; fortuitously, the actual defocus and astigmatism values left all the observable reflections strongly transferred in CTF bands with the same contrast (Figure 4), and thus no phase correction was necessary in the present case.

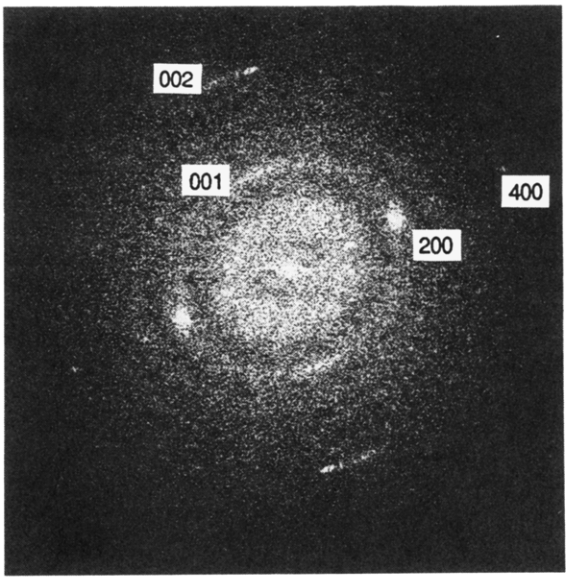

Figure 4. Power spectrum, equivalent to the square of the modulus of the Fourier transform, from a portion of the digitized image used for subsequent processing with Semper. Reflections from 001, 002, 200, 400, and 202 were used in subsequent image processing. All but 202 are reproduced in the print.

Fourier filtering is known[10,27] to introduce a number of artifacts in the reconstructed image unless great care is taken in the selection and application of the filter. The FT of the image is first computed and regions of the spectrum around the diffracted peaks are selected via a *window* filter for subsequent inverse transformation back to an image. The technique selects the periodic signal in the image and rejects the majority of the background noise. Windows in the filter were placed only over reflections in the power spectrum which were significantly above the noise level and which were also present in selected-area diffraction patterns. This is to prevent windows containing only noise from appearing to create structural information from a spatial frequency that was not present in the original image. Similarly, only areas containing clear high-resolution fringes were filtered to avoid the production of a spurious "ghost lattice" from the noise in the spectrum in areas of the processed image where no lattice was visible in the original. The filter window size was used to control the image area averaged: a window size of $1/n$ of the lattice spacing averages the filtered image over ~n lattice motifs.[27] The value for n used here was 4.

In Fourier synthesis, the amplitude and phase of each Fourier component of the crystal are determined by direct examination of the neighborhood of the corresponding reflection in the calculated transform. The components are then resynthesized to form an image. This technique is ideal for well-crystallized areas of image; one unit cell is computed from which larger regions may be built up.

Results and Discussion

High-Resolution Images. The high-resolution images obtained showed lattice fringes in patches, typically 20–50 nm in diameter (both parallel and perpendicular to the chain direction) covering up to 50% of the micrograph. A typical image is shown in Figure 5. The maximum length of an individual, continuous lattice fringe in the direction parallel to the chain backbone was found to be between 40 and 50 nm; this compares to an expected chain length of ~100 nm derived from the provisional molecular weight measurements and an estimated repeat unit length based on standard bond lengths. This discrepancy probably

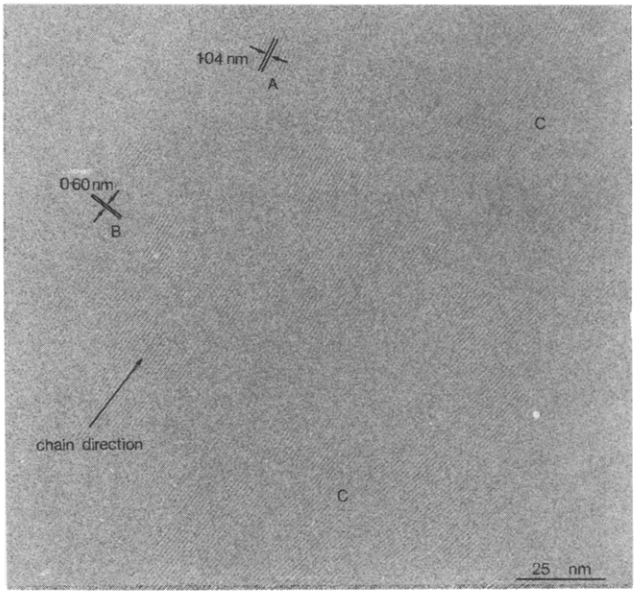

Figure 5. High-resolution image recorded at 120 kV, without an objective aperture. Regions of ~50-nm diameter containing continuous lattice fringes are visible, plus numerous faults in the chain packing. Fringe spacings of 1.04 nm (e.g., at A) and 0.60 nm (e.g., at B) may be seen by eye. Crossed fringes are present in some areas, e.g., at C. The fringes may be seen more clearly by viewing the page at a glancing angle.

reflects the difficulty of crystallizing the polymer over large distances in the very short crystallization time available during evaporation of the solvent rather than large inaccuracies in the molecular weight determination, as a 50-nm maximum crystallite dimension was observed both parallel and perpendicular to the chain direction. Crystallites were defined as areas showing clear high-resolution fringes with no substantial change in fringe direction. The crystallites did not exhibit any strong shape anisotropy.

Bends and undulations in the fringes parallel to the chain direction were visible in many places on the micrographs, as shown in Figure 5. Bends of up to 5° were frequently seen in these nominally rigid-rod chains. Again, this probably reflects the constraints of rapid crystallization. Significant variations in overall crystallite orientation were seen across the specimen as a whole, as illustrated in Figure 6, which shows the outline and chain direction of a group of crystallites (of which Figure 5 forms a part), but the order parameter for areas recorded on an individual micrograph could be very high. An order parameter of 0.97 was calculated for the 37 crystallites shown in Figure 5. The order parameter is defined as the mean value of $(3\cos^2\theta - 1)/2$, where θ is the angle between the chain direction in a crystallite and the average chain direction.

The images are similar in many respects to those obtained from poly(*p*-phenylenevinylene) (PPV) films in the work by Masse et al.,[17] where crystallites of ~5-nm diameter with an order parameter of 0.94 and local misorientations between crystallites of up to ~11° were observed. In this material we observed larger crystallites (~50 nm) with smaller local misorientations (≤5°) and a higher order parameter (0.97). Masse et al.[17] proposed a micellar model of interconnected crystallites for PPV as consistent with its good mechanical properties. The materials studied here have not been produced in sufficiently large quantities for mechanical testing. The bulk solid is generally brittle and weak but the cast films were often found to be strong in that the ≤20-nm-thick films did not break easily during collection as small sections on

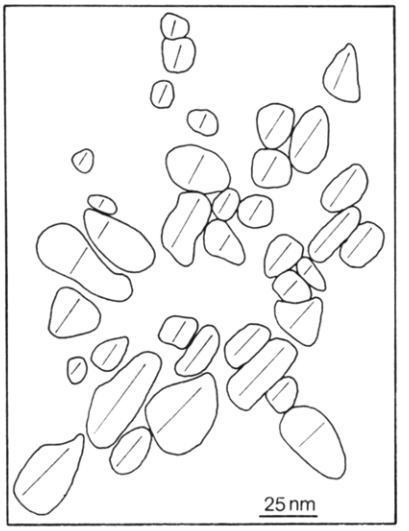

Figure 6. Diagram illustrating the size, position, and chain direction of individual microcrystallites including those shown in Figure 5. A microcrystallite is defined as an area showing continuous, undistorted lattice fringes. For this area the order parameter is 0.97.

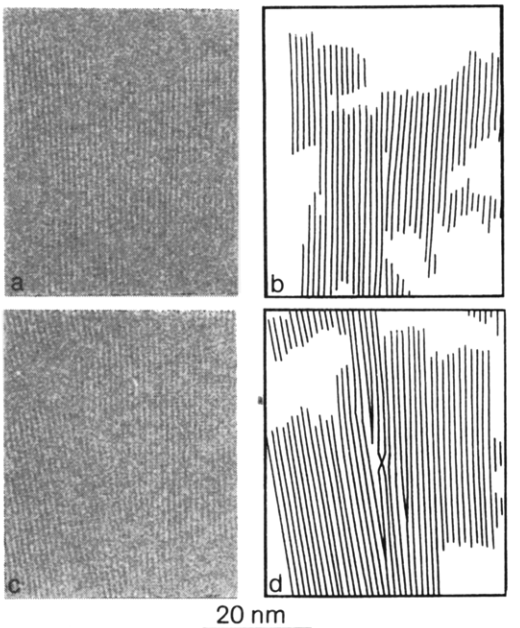

Figure 7. Two regions, from the HREM micrograph shown in Figure 5, and their corresponding line tracings produced by following bright fringes in the print. In (a) and (b), a fault, apparently an edge dislocation, is visible. In (c) and (d), more complex faults and chain bending are visible. Direct interpretation of these images is not possible as they are formed by a projection of stacked chains of ~10 molecules.

TEM grids. From the HREM images and the mechanical behavior of the films it thus seems likely that their microstructure may also consist of interconnected micelles.

Dislocation-type defects and grain boundary regions were seen in the images. Figure 7 shows two areas from the large micrograph in Figure 5 with accompanying line tracings. The line tracings were taken by following the light fringes on the print; one shows an apparently conventional edge dislocation but the second shows more complex defects, including a region where chains *appear* to cross over each other. However, it must be remembered that these HREM images are projections through a film of ≤20-nm thickness, i.e., at least ten molecules thick, and thus direct interpretation of these images is oversimplistic. The appearance of crossing fringes in the image does

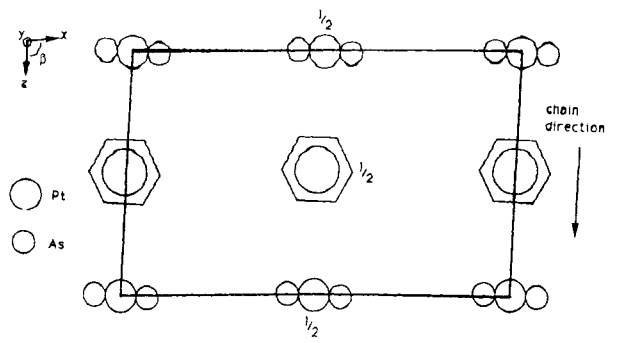

Figure 8. Proposed unit cell for the Pt–As polyyne, showing the positions of the Pt and As atoms only; $a = 2.08$ nm, $c = 1.20$ nm, $90° \leq \beta \leq 93°$, and $b \sim 1.9$ nm. Chains are stacked with the plane of the As–Pt–As segments and the benzene rings lying in the x–z plane.

not necessarily imply a crossover in the parallel stacks of polymer chains. The use of image processing to clarify defects is also difficult; Fourier filtering techniques average out image detail and thus distort the area around the defect but it is hoped that use of maximum entropy-based algorithms[28] and image simulation will clarify our understanding of defect images.

Regions of the micrographs showing lattice fringes fell into a number of distinct categories: regions with either 0.60- or 1.04-nm fringes; regions with crossed fringes at approximately 90°; regions with distinct faults, boundaries, or textures reminiscent of twinning. Image areas with 0.60-nm fringes often showed the fringes associated in pairs (i.e., alternate fringes appeared to be closer together) although optical diffractometry always indicated a regular 0.60-nm spacing. Image processing assisted in understanding this observation, as will be discussed further in the next section. A range of image types is illustrated in Figure 5. The generally low signal-to-noise ratio of the raw images makes detailed interpretation of the data difficult; image processing was used to improve the quality of the data for crystal structure determination.

Variations in the structure seen across one micrograph could reflect a combination of factors: local changes in orientation present in the film, the effects of local specimen movement under the electron beam and, possibly, localized beam damage. The first effect is likely to be the predominant one, and this is borne out by the observation that many of the SADP's showed some reflections from out of the $h0l$ plane (Figure 1).

Two-Dimensional Structure Determination. Structure determination by electron microscopy for a beam-sensitive polymer is not a simple task. In this case there are no X-ray diffraction data as single crystals could not be grown but we have used the flexibility of electron microscopy for dealing with very small crystallites. Information from the SADP's, high-resolution images, and details of the repeat unit can, in principle, all be combined to give a preliminary estimate of the structure. Initial work[3] indicated a two-dimensional unit cell with $c = 1.20$ nm, $a = 2.08$ nm, and $\beta = 90°$ and is similar in many respects to the newly proposed unit cell shown in Figure 8. In this work we have refined our description of the unit cell but have also uncovered some ambiguities which will be discussed in the last part of this section.

SADP's from large areas of film showed crisp but very short-lived reflections, often with very high symmetry. The best patterns were usually recorded from areas of film which subsequent examination in image mode showed had been slightly stretched during collection of the sample from the water surface, as indicated by the observation of elongated, slightly folded, or wrinkled regions of film seen at low magnifications (~5000×). Of the two examples shown in Figure 1, that recorded from the more heavily stretched region (Figure 1b) shows better orientation as the degree of arcing is considerably reduced. These diffraction patterns indicate an orthorhombic cell, as before. Some of the reflections appear to be of the type hkl; i.e., a proportion of crystallites included in the pattern were rotated about the z-axis so that reflections out of the $h0l$ plane were visible. In addition to smaller arcs, Figure 1b shows fewer and weaker hkl reflections, thus supporting the hypothesis that stretching produces better overall orientation in the film.

As shown in Figure 1 it has been possible to index virtually all of the reflections using a value of $b \sim 1.9$ nm but this assignment is, at best, tentative as the only $0k0$ reflection seen in the patterns was 080 whereas the structure resulting from these lattice parameters whould also show 020, 040, etc.

Electron diffraction from materials ordered over small distances suffers from severe limitations in the accurate determination of angular lattice constants; the diffraction pattern shown in Figure 2 was recorded from the smallest feasible area of the specimen, equivalent to ~0.5 μm in diameter. This area still includes several microcrystalline regions in a variety of orientations and thus the overall diffraction pattern shows arcs rather than discrete spots. Optical diffractometry of recorded images improves the selectiveness down to areas ~100 nm in diameter (Figure 3) but the use of computed power spectra from small regions of digitized images offers the most powerful approach and allowed us to select individual microcrystallites. The power spectrum shown in Figure 4 was computed for one crystallite over 64 × 64 pixels and shows well-defined peaks corresponding to the $h00$ reflections and small arcs for the $00l$ reflections. From a series of ten such spectra, each calculated for an individual crystallite, the best value of β^* was measured at ~87°, thus leading to a monoclinic unit cell with $\beta \sim 93°$.

Image reconstruction using filtering techniques with phase and amplitude correction has, as described earlier, led to considerable improvements in structure determination by electron microscopy. We have applied this technique to our data, taking precautions to avoid the pitfalls associated with crystal edges and defects.[10,27] Phase assignment was straightforward as the degree of image defocus and astigmatism in the image used in processing (530 ± 7 and 150 ± 7 nm, respectively) resulted in all the reflections recorded in the image having the same phase as transferred by the CTF. Accurate amplitude correction could not be applied, as mentioned earlier, and therefore the reconstructed, filtered images must be viewed with caution for structure determination as the CTF dominates the information. However, the filtered images were found useful in assessing features originally observed on the negatives.

Window-filtered and Fourier-synthesized images from one crystallite are shown in Figure 9. Both images show the main 0.6- and 1.04-nm fringes more clearly than the original, unprocessed image and contain similar features; the most electron dense (black) areas are seen with an apparent spacing of 1.2 nm along the chain direction, with slightly less dense regions lying between them. The alternation of intensity of these groups creates the impression of pairing that was observed in the original images. The Fourier-synthesized image is more regular and less noisy than the window-filtered image as this synthesis technique takes only one point in reciprocal space at the center of each reflection whereas the window-

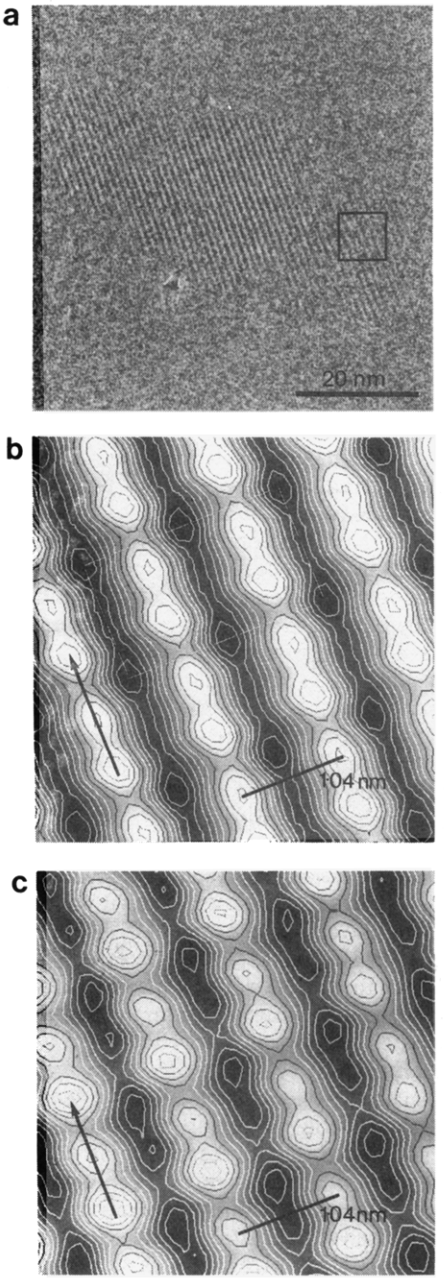

Figure 9. (a) Electron micrograph of the image area digitized for processing on Semper, showing the area from which the power spectrum in Figure 4 was calculated and on which processing was carried out. (b) Fourier-synthesized image of (a) using the amplitudes and phases of the 001, 002, 200, 400, and 202 reflections. Atoms are shown in black with white contours, and electron-deficient areas are shown in white with black contours. The chain direction is indicated by the arrow, and the unit cell is outlined in white. (c) Window-filtered image of (a) using windows of 0.25× the lattice parameters over the same reflections used in (b). Same contrast as (b). The processed images show greater detail than the original image; the variation in intensity of alternate groups of As–Pt–As atoms and the consequent pairing of electron-deficient areas are clearly seen. The chain direction is indicated by the arrow.

filtering technique used windows with a diameter of one-quarter of the reciprocal lattice vectors, thus allowing more noise to contribute to the final result.

The reconstruction used two strong reflections along z^*, all with the same phase. Addition of two sine waves with the same phase but with one wave having half the wavelength of the other will result in a total wave showing alternating small and large maxima. Thus, the inclusion of only two $00l$ reflections automatically results in the appearance of alternating maxima and hence pairing of fringes in the image. This effect cannot necessarily be deduced to relate to structural units in the unit cell: the limited resolution and lack of true amplitude information prohibit such simplistic conclusions.

Nevertheless, using the information in the SADP's and the regular grid seen in the high-resolution images we can make an initial attempt at fitting the known repeat unit of the molecule into a cell which conforms to all the available data. Various structures have been assessed by calculating structure factors based on the expected positions of the most electron dense parts of the molecule within the trial cells. The As–Pt–As groups and the benzene rings have been included, but the flexible *n*-butyl chains have been disregarded as these include a large number of atoms with uncertain positions and will probably not contribute greatly to the diffraction spots. The unit cell giving the best qualitative fit to the SADP intensities is shown in Figure 8 and comprises a *C*-centered cell (the reflections indicate a systematic absence of $h + k = 2n$) with the plane of the As–Pt–As groups and the benzene rings contained in the x–z plane. The As–Pt–As groups are situated at the corners of the cell and in the center of the 001 planes and thus $a = 2.08$ nm and not 1.04 nm which is the spacing of the stacks of molecules as seen in the HREM images.

Initial work using molecular modeling[29] suggests that the polymer chains can pack easily in the manner proposed in Figure 8; the *n*-butyl chains are not forced into overlaps with other groups, and the closest reasonable lateral packing of chains gives a spacing that conforms with our experimentally determined value of a. It is hoped to make further use of modeling to define likely positions for all the atoms in the unit cell and use these for more accurate calculations of the expected structure factors.

A number of ambiguities still remain; a value of b has been calculated but gives rise to some unusual indexing in the diffraction patterns (080 is present but not 020, 040, etc.), and the value of β as measured in the power spectra is inconsistent with features of the SADP's. These two problems are related. The hkl and the $0kl/0k0$ reflections in the SADP's are thought to arise from rotations of some crystallites about the z-axis (the chain direction); i.e., we see fiber symmetry introduced by light stretching of the film. The value of β that was obtained from the power spectra from individual crystallites indicated a monoclinic unit cell, but fiber symmetry in a monoclinic system would produce a diffraction pattern very different from those actually observed. Thus, we have two results, each apparently unambiguous and yet incompatible with each other although having been recorded from the same specimen.

This problem can be overcome by considering the nature of this polymer; the flexible side chains and the relatively open packing are likely to make it amenable to orientation by stretching and able to accommodate slightly different values of β. This is borne out by the observation that even for the power spectra from individual crystallites the $00l$ reflections were always seen as arcs. Thus, the rigidity of the chain backbone ensures that the $h00$ planes are well defined in any one crystallite but there is still flexibility in the exact registration of neighboring chains and hence in the definition of β and therefore the $00l$ reflections form as arcs.

The sample used in this work did fulfill the criteria for application of the weak phase object approximation and image reconstruction. If future low-dose images could be recorded with higher resolution and if diffracted ampli-

tudes can be measured from typical image areas with certainty, then much more structural detail about the unit cell could be revealed using this approach. One possible route for gaining improved resolution would be the spot scan imaging technique developed by Downing and Glaeser[30,31] in which the loss of information through local specimen distortions is minimized during the exposure. Other methods which could further our understanding of these high-resolution images are image processing with a maximum-entropy algorithm,[28] which provides an unbiased approach to the analysis of images containing discontinuities, and correlation averaging,[5] which provides averaged images free from the effects of specimen distortion.

Summary

Low-dose techniques have succeeded in providing high-resolution structural and microstructural information from a Pt–As-containing polyyne at liquid nitrogen temperatures. Crystallites with a diameter of ~50 nm were seen over large areas of the specimens, and a number of faults, e.g., chain bending, dislocations, and grain boundaries, were observed. A combination of information from electron diffraction, lattice images, and knowledge of the repeat unit has yielded a refined unit cell with parameters a, c, and β known (20.8 nm, 1.20 nm, and $90° \leq \beta \leq 93°$, respectively) and a tentative assignment of b at ~1.9 nm. The variation in β appears to arise from the openness of the packing and the tendency of the polymer to align on stretching.

Acknowledgment. We are indebted to many people for their assistance and advice in various areas of this work: Dr. R. Henderson and Dr. N. Unwin of the MRC Laboratory of Molecular Biology for the use of electron microscope facilities; Dr. T. Nicolai and Dr. P. Johnson for the molecular weight measurements; Dr. J. Barna of the Department of Biochemistry, University of Cambridge, for the molecular modeling; and Dr. R. Payne of the Cavendish Laboratory and the ICI Wilton Research Center for the parallel electron energy loss spectroscopy measurements. We also acknowledge the support of the Science and Engineering Research Council (for A.E.D. and M.S.K.) and thank Dhaka University (Bangladesh) for study leave for M.S.K.

References and Notes

(1) Takahashi, S.; Kariya, M.; Yatuke, K.; Sonogashira, K.; Hagihara, N. *Macromolecules* **1978**, *11*, 1063.
(2) Hagihara, N.; Sonogashira, K.; Takahashi, S. *Adv. Polym. Sci.* **1981**, *41*, 151.
(3) Dray, A.; Wittmann, F.; Friend, R.; Donald, A.; Khan, M. S.; Lewis, J.; Johnson, B. F. G. *Synth. Met.* **1991**, *41–43*, 871.
(4) Unwin, P. N. T.; Henderson, R. *J. Mol. Biol.* **1975**, *94*, 425.
(5) Saxton, W. O.; Baumeister, W. *J. Microsc.* **1982**, *127* (Part 2), 127.
(6) Fryer, J. R.; Smith, D. J. *Proc. R. Soc. London* **1982**, *A381*, 225.
(7) Fryer, J. R.; Holland, F. *Proc. R. Soc. London* **1984**, *A383*, 353.
(8) Fryer, J. R. *Ultramicroscopy* **1984**, *14*, 227.
(9) Fryer, J. R. *Ultramicroscopy* **1987**, *23*, 321.
(10) Pradere, P.; Revol, J. F.; Nguyen, L.; St. John Manley, R. *Ultramicroscopy* **1988**, *25*, 69.
(11) Young, R. J.; Yeung, P. H. J. *J. Mater. Sci. Lett.* **1985**, *4*, 1327.
(12) Voigt-Martin, I. G.; Durst, H. *Liq. Cryst.* **1987**, *2* (5), 585.
(13) Voigt-Martin, I. G.; Durst, H. *Liq. Cryst.* **1987**, *2* (5), 601.
(14) Voigt-Martin, I. G.; Durst, H. *Macromolecules* **1988**, *21*, 1626.
(15) Voigt-Martin, I. G.; Durst, H. *Macromolecules* **1989**, *22*, 168.
(16) Revol, J. F.; Chanzy, H. D.; Deslandes, Y.; Marchessault, R. H. *Polymer* **1989**, *30*, 1973.
(17) Masse, M. A.; Martin, D. C.; Thomas, E. L.; Karasz, F. E.; Petermann, J. H. *J. Mater. Sci.* **1990**, *25*, 311.
(18) Johnson, B. F. G.; Kakkar, A. K.; Khan, M. S.; Lewis, J.; Dray, A. E.; Wittman, F.; Friend, R. H. *J. Mater. Chem.* **1991**, *1* (3), 485.
(19) Khan, M. S.; Davies, S. J.; Kakkar, A. K.; Schwartz, D.; Lin, B.; Johnson, B. F. G.; Lewis, J. *J. Organomet. Chem.*, in press.
(20) Nicolai, T., private communication.
(21) Johnson, P., private communication.
(22) Hayward, S. B.; Glaeser, R. M. *Ultramicroscopy* **1979**, *4*, 201.
(23) Reimer, L. *Transmission Electron Microscopy: Physics of Image Formation and Microanalysis*; Springer-Verlag, Berlin, 1989.
(24) Dray, A. E.; Rachel, R.; Saxton, W. O.; Donald, A. M.; Friend, R. H.; Khan, M. S.; Lewis, J., *Ultramicroscopy*, in press.
(25) Buseck, P.; Cowley, J.; Eyring, L. *High Resolution Electron Microscopy*; Oxford University Press: Oxford, 1988.
(26) Saxton, W. O.; Pitt, T. J.; Horner, M. *Ultramicroscopy* **1979**, *4*, 343.
(27) Pradere, P.; Thomas, E. L. *Ultramicroscopy* **1990**, *32*, 149.
(28) Anderson, D. M.; Martin, D. C.; Thomas, E. L. *Acta Crystallogr.* **1989**, *A45*, 686.
(29) Still, W. C.; Mohamadi, F.; Richards, N. G. J.; Guida, W. C.; Lipton, M.; Liskamp, R.; Chang, G.; Hendrickson, T.; DeGunst, F.; Hasel, W. MacroModel V2.5, Department of Chemistry, Columbia University, New York, NY, 10027.
(30) Downing, K. H.; Glaeser, R. M. *Ultramicroscopy* **1986**, *20*, 269.
(31) Downing, K. H. *Science* **1991**, *251*, 53.